Proc. Natl. Acad. Sci. USA
Vol. 95, pp. 10832–10835, September 1998
Medical Sciences

In vivo magnetic resonance vascular imaging using laser-polarized ^{3}He microbubbles

MARK S. CHAWLA*, X. JOSETTE CHEN, HARALD E. MÖLLER, GARY P. COFER, C. TED WHEELER, LAURENCE W. HEDLUND, AND G. ALLAN JOHNSON

Center for *In Vivo* Microscopy, Duke University Medical Center, Durham, NC 27710

Communicated by William Happer, Princeton University, Princeton, NJ, July 13, 1998 (received for review March 16, 1998)

ABSTRACT **Laser-polarized gases (^{3}He and ^{129}Xe) are currently being used in magnetic resonance imaging as strong signal sources that can be safely introduced into the lung. Recently, researchers have been investigating other tissues using ^{129}Xe. These studies use xenon dissolved in a carrier such as lipid vesicles or blood. Since helium is much less soluble than xenon in these materials, ^{3}He has been used exclusively for imaging air spaces. However, considering that the signal of ^{3}He is more than 10 times greater than that of ^{129}Xe for presently attainable polarization levels, this work has focused on generating a method to introduce ^{3}He into the vascular system. We addressed the low solubility issue by producing suspensions of ^{3}He microbubbles. Here, we provide the first vascular images obtained with laser-polarized ^{3}He. The potential increase in signal and absence of background should allow this technique to produce high-resolution angiographic images. In addition, quantitative measurements of blood flow velocity and tissue perfusion will be feasible.**

Conventional MRI derives its signal predominantly from the hydrogen nuclei in the water molecules of body tissues. Higher signal levels may be obtained with laser-polarized gases (^{3}He and ^{129}Xe), which can be introduced to regions previously lacking a proton signal source. Polarizing noble gases by the spin exchange method has been described in detail previously (1–3). Briefly, valence electrons in a rubidium vapor are optically pumped with circularly polarized laser light. Through collisional spin exchange, angular momentum is transferred to the noble gas nuclei. This process increases nuclear polarization, and thus magnetic resonance signal, up to 10^5 times the thermal equilibrium value. Even after considering the lower density of gas relative to water, the conventional signal source in MRI, the signal-to-noise ratio (SNR) of a laser-polarized ^{3}He image can be improved to 20 times that of a standard proton image (assuming equivalent volumes in a 2 T magnetic field) (3). Since ^{3}He and ^{129}Xe do not occur naturally in the body, laser-polarized gas images contain no background signal. As a result, the contrast-to-noise ratio of an image is improved even more dramatically than the SNR.

This increased SNR has enabled quality images of void spaces, notably the lungs, to be acquired with both gases (3–11). Recently, imaging blood (12), muscle (13), and brain tissue (14) using ^{129}Xe has been explored. Because xenon dissolves in the pulmonary blood after inhalation, it can be transported to a location of interest by the vascular system. Alternatively, it may be predissolved in some vehicle, such as a lipid-rich material, which is subsequently injected. Since helium is 10–100 times less soluble than xenon in these substances (15), ^{3}He has been used exclusively for airspace imaging. However, because of its larger magnetic moment and higher presently attainable polarization level, ^{3}He provides a factor of 10 improvement in signal over that of ^{129}Xe (3). We describe here techniques that utilize this extraordinary signal gain to generate ^{3}He images of both the arterial and venous systems of a live rat.

To overcome the low solubility issue, ^{3}He was suspended within microbubbles. It is essential to preserve the ^{3}He polarization while these bubbles are suspended and prepared for injection. Due to the nonequilibrium nature of the magnetization, it decays with a characteristic time (longitudinal relaxation time or T_1) that depends on its interaction with the surrounding environment. Paramagnetic materials, including oxygen and various metals, rapidly depolarize the gas. The number and size of the bubbles containing polarized gas and the time that they remain within the fluid are all directly related to the SNR that can be obtained. According to Stokes' law, characteristics of the suspending fluid, including surface tension, density, and viscosity, affect the bubble size distribution and the rate at which the bubbles rise out of the suspension. Thus, the technique of bubble suspension, along with any materials involved, must be carefully chosen to ensure that high signal will remain throughout the imaging process.

MATERIALS AND METHODS

Bubble Production. Using methods described previously (3), ^{3}He was polarized to 10–15% using a 120 W fiber-coupled diode laser array (polarizer, Magnetic Imaging Technologies, Inc., Durham, NC; laser, OptoPower Corp., Tucson, AZ). An evacuated glass holding cell was connected to the polarizing cell and then filled to ≈2 atmosphere. Two cubic centimeters of gas (at 1 atmosphere = 101.3 kPa) were withdrawn from this holding cell into an evacuated 10-cm^3 plastic syringe. Removal of air is critical to prevent the paramagnetic oxygen from depolarizing the ^{3}He (16). This syringe was then connected, via a plastic three-way stopcock, to a second 10-cm^3 syringe containing 8 cm^3 of fluid. The fluid was rapidly flushed several times between the syringes in a manner similar to that done in contrast echocardiography (17), producing a suspension of ^{3}He microbubbles.

Choice of Suspending Fluid. We tested four commercially available radiographic contrast agents (Hexabrix, Mallinckrodt; Omnipaque, Winthrop Pharmaceuticals, New York, NY; Renografin and Isovue, both from Squibb) and two plasma volume expanders (dextran and Hetastarch, Abbott) in search of an injectable vehicle with minimal pharmacological effects that would contain enough ^{3}He to produce the necessary SNR for *in vivo* imaging. Syringes containing bubbles suspended in each fluid were placed in the magnet and imaged. The time between agitation and image acquisition (≈10 s) was the same

The publication costs of this article were defrayed in part by page charge payment. This article must therefore be hereby marked "*advertisement*" in accordance with 18 U.S.C. §1734 solely to indicate this fact.

Abbreviations: RF, radio frequency; SNR, signal-to-noise ratio; TR, repetition time.

*To whom reprint requests should be addressed at: Center for *In Vivo* Microscopy, Duke University Medical Center, Box 3302, Durham, NC 27710. e-mail: msc@orion.mc.duke.edu.

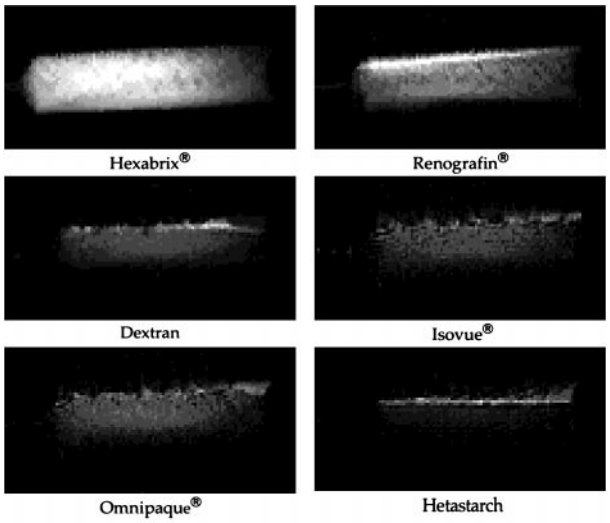

FIG. 1. Phantom images (non–slice-selective sagittal orientation) of ^{3}He microbubbles suspended in six biologically compatible fluids. Note the range of signal intensity and homogeneity among the liquids. Hexabrix was chosen for the *in vivo* studies based on the high signal (SNR = 136) and homogeneously distributed bubbles.

for both phantom and *in vivo* imaging. The quality of the images indicated the various fluids' potentials for imaging blood vessels *in vivo*.

Bubble Size Distribution. The approximate size distribution of suspended ^{3}He microbubbles was determined using a Coulter Counter (Z2 model, Coulter). ^{4}He was used for this work rather than the more expensive ^{3}He. The instrument was fitted with a 100-μm aperture, which accurately sizes diameters from 2 to 60 μm. Two analyses were performed at both small and large diameter counting regions and results were averaged. The counting process takes 12.5 s, during which time larger bubbles rise out of the liquid more quickly than smaller bubbles. Thus, the distribution underestimates the proportion of large diameter bubbles.

Animal Preparation. All animal procedures were approved by the Duke University Institutional Animal Care and Use Committee. *In vivo* imaging was performed with male rats (Harlan–Sprague–Dawley) weighing between 400 and 480 g. Anesthesia was maintained with either pentobarbital sodium (Abbott) or isoflurane (Aerrane, Ohmeda Caribe, Guayama, Puerto Rico), and euthanasia was performed with an anesthetic overdose. For venous injections, a 22-gauge plastic cannula (Sherwood Medical Industries, Tullamore, Ireland) was inserted into a lateral tail vein; for arterial injections, a catheter (PE 50 tubing, Becton Dickinson) was inserted into the aorta via the left carotid artery. Immediately after creating the ^{3}He microbubble suspension, 7 cm^3 [≈25% of the total blood volume (18)] was injected into the animal.

Magnetic Resonance Procedures. All magnetic resonance experiments were performed on a 2.0 T, 30-cm-bore magnet (Oxford) with shielded gradients (180 mT/m) using a Signa console (General Electric). The animal was placed in the supine position inside a custom-built dual-frequency 7-cm-diameter birdcage radio frequency (RF) coil operating at 65.1 MHz and 85.5 MHz for ^{3}He and ^{1}H, respectively. All ^{3}He imaging employed a standard two-dimensional gradient-recalled echo pulse sequence (19) with the following parameters: 79-mm field-of-view, coronal plane with no slice selection, 128 × 256 matrix size zero-filled to 256 × 256, 1.2 ms effective echo time, 80 or 200 ms repetition time (TR), and 15 or 20° flip angle (α). Injections lasted either 10 or 26 s (corresponding to 128 excitations with a TR of either 80 or 200 ms), during which imaging occurred. The phantom imaging, which did not involve flow, used similar parameters, but with a 6 ms TR and 11° α. The sagittal orientation was chosen for these images so that it would be possible to determine whether bubbles had ascended to the top of the syringes. After the ^{3}He study, ^{1}H angiography was performed using a three-dimensional time-of-flight sequence (20) with 79-mm field-of-view, coronal plane, 192 × 256 matrix size zero-filled to 256 × 256, 2.2 ms echo time, 18 ms TR, 30° α, 2 excitations, and 0.7-mm slice thickness.

Table 1. SNR comparison of ^{3}He microbubbles suspended in various fluids

Fluid	Relative SNR
Hexabrix	1.00 ± 0.19
Renografin-76	0.53 ± 0.16
Dextran 40 + 5% dextrose	0.28 ± 0.09
Isovue-300	0.15 ± 0.04
Omnipaque 350	0.14 ± 0.02
6% Hetastarch	0.14 ± 0.03

Values relative to the Hexabrix SNR.

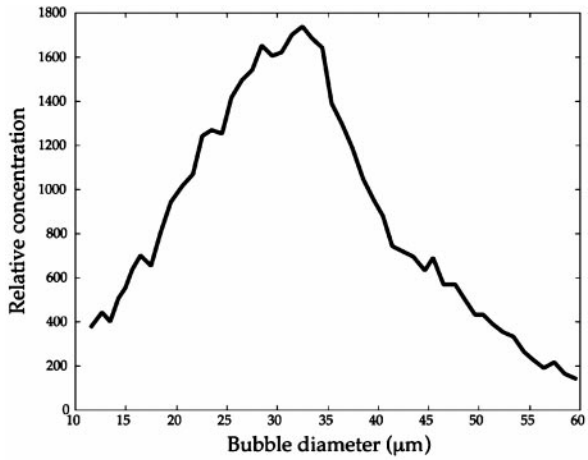

FIG. 2. Approximate size distribution of ^{3}He microbubbles suspended in Hexabrix. The mean bubble diameter is 31.8 μm and the SD is 10.4 μm.

To measure T_1, the polarization of ^{3}He suspended in a syringe was sampled with small flip angle RF pulses (≈5°). Because signal loss occurs as a result of T_1 decay and RF excitations, the signal acquired on the nth excitation is given by: $S(n) \propto M_o \sin \alpha \, (e^{-TR/T1} \cos \alpha)^{n-1}$, where S is the signal voltage and M_o is the initial magnetization. The data were fit to the equation with a nonlinear least-squares method. Because a precise measurement of the flip angle is often difficult to accomplish, α was eliminated from the equation by performing multiple experiments using the same flip angle but different repetition times (0.25–5 s). In each case, data were acquired for 45 s. Throughout the experiment, bubbles rose to the top of the sample and coalesced. A coronal slice encompassing the lower portion of the syringe was chosen to acquire signal only from gas still suspended in the fluid. Thus, this measured signal decay time, $T_{1,measured}$, includes the decay due to both the loss of longitudinal magnetization, given by $T_{1,actual}$, and bubbles rising out of the slice, given by T_{rise}: $1/T_{1,measured} = 1/T_{1,actual} + 1/T_{rise}$.

RESULTS AND DISCUSSION

Representative phantom images of ^{3}He suspended in the six fluids are shown in Fig. 1. Notice the wide range of signal intensities and degrees of homogeneity provided by the different liquids. For example, the entire volume of the syringe containing Hexabrix appears bright, while only the upper surface of the Hetastarch is visible. This horizontal line present

in some of the images occurs if the bubbles quickly rise to the surface of the liquid before the image is acquired. The relative SNRs achieved with these fluids are presented in Table 1. Imaging with Hexabrix resulted in almost twice the SNR than with any other liquid. Thus, it was chosen as the suspending medium for *in vivo* vascular imaging.

Fig. 2 shows the size distribution of the bubbles suspended in Hexabrix. The mean bubble diameter is 31.8 μm, while the SD is 10.4 μm. As expected, the hand-agitation technique of suspending microbubbles resulted in significant variability of bubble size. Various current methods, including sonication, are capable of producing smaller, more uniform microbubbles (21). However, hand-agitated bubbles were sufficient for this preliminary feasibility study. Measurement of the combined effects of depolarization and rising bubbles in a phantom yielded an effective decay time of 41.6 $\pm$ 8.7 s for Hexabrix. This value is a lower limit of the actual T_1 and indicates adequate magnetization will persist throughout the mixing and delivery process.

Images of both the arteries (Fig. 3*a*) and veins (Fig. 3*b*) of the rat pelvic region were obtained using ^{3}He microbubbles suspended in Hexabrix. Excellent delineation of all major vessels can be seen, with a maximum SNR $\approx$ 55 in both images. For Fig. 3*a*, the injected microbubbles traveled downward through the abdominal aorta (top of the image), branched into the common iliac arteries, and finally passed through the external iliac arteries. For the venous image, the injection site was a lateral tail vein. Due to collateral circulation, the suspension could travel a circuitous route through the vessels. As a result, multiple veins are observable in Fig. 3*b*. From the bottom to the top of the image, which is the direction the bubbles flowed, the caudal veins, common iliac veins, and vena cava are visible.

Fig. 4 includes a non–slice-selective ^{3}He image (SNR $\approx$ 20) (*a*) and a corresponding ^{1}H image (*b*) of the rat abdominal region. The outline of the kidneys in the upper portion of Fig. 4*b* provides some anatomical reference. In this region on both images, the right and left renal arteries originate from the abdominal aorta, which is the prominent vertical vessel. In Fig. 4*a*, the superior mesenteric artery arises from the same location as the right renal artery. However, this vessel is not present in Fig. 4*b* because it is not oriented in the slice direction and the image is only a small section (4.9 mm) from a three-dimensional data set. The vena cava can be seen in the lower portion of the ^{1}H image. Based on its similar position, we believe the faint line running parallel to the aorta in the ^{3}He image is also the vena cava. This means sufficient amounts of polarized ^{3}He bubbles reached the venous circulation. The absence of the vena cava in Fig. 3*a* is a result of the ^{3}He being depolarized while still in the arterial system. This was caused by using a larger flip angle (20° vs. 15°) and a shorter repetition time (80 ms vs. 200 ms). RF pulses associated with image acquisition necessarily depolarize the ^{3}He. Therefore, the RF power (i.e., flip angle), repetition time, and injection rate must be carefully chosen to ensure that sufficient magnetization will remain throughout the region of interest (22, 23). In this situation, an image containing both arteries and veins or an image containing exclusively arteries may be obtained.

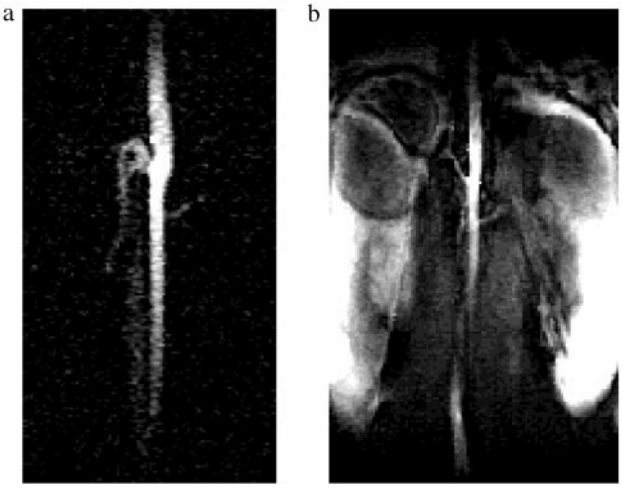

FIG. 4. (*a*) *In vivo* non–slice-selective coronal image of the renal arteries in a rat acquired using ^{3}He microbubbles suspended in Hexabrix (0.31 $\times$ 0.31 mm resolution, 200 ms TR, 15° α). The following vessels are present: abdominal aorta, superior mesenteric artery, right and left renal arteries, and vena cava. (*b*) A 4.9-mm coronal section (seven slices) from a three-dimensional ^{1}H image of the same location (0.31 $\times$ 0.31 mm in-plane resolution).

Using a suspension of microbubbles to overcome the limited solubility of helium, we have created a novel signal source and acquired vascular images with laser-polarized ^{3}He. The contrast mechanism used here is quite different from that which is typically used in MRI. Standard contrast agents, such as gadolinium-diethylenetriamine pentaacetic acid, affect the relaxation of the original signal source, whereas this contrast agent is the signal source.

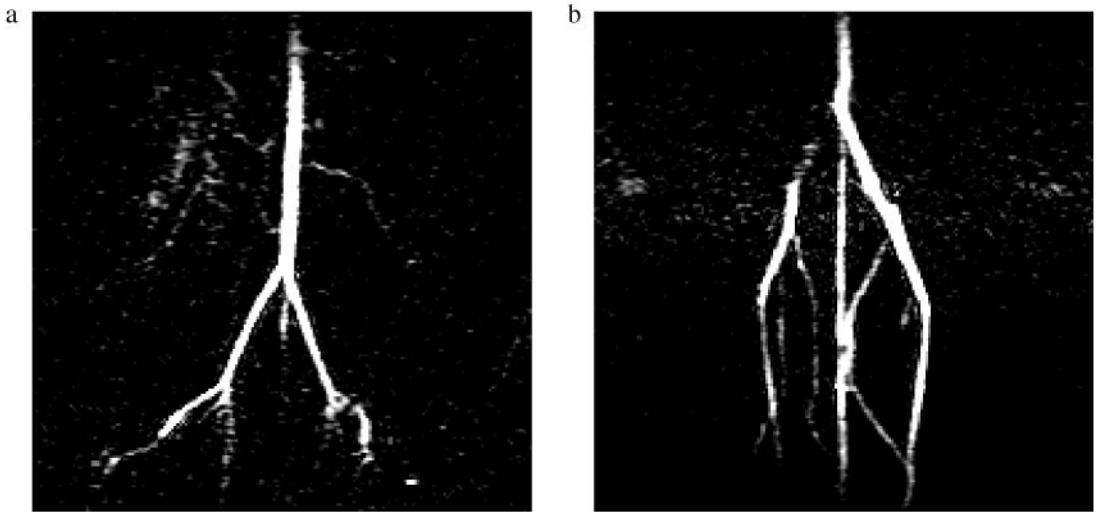

FIG. 3. *In vivo* non–slice-selective coronal images (0.31 $\times$ 0.31 mm resolution, 80 ms TR, 20° α) of rat vasculature acquired using ^{3}He microbubbles suspended in Hexabrix. The imaging region of *a* is several centimeters cranial to the location of *b*. In *a*, the abdominal aorta, common iliac, and external iliac arteries are observable, and in *b*, the vena cava, common iliac, and caudal veins are visible.

Although hand-agitated bubbles have been used in myocardial contrast echocardiography for years, the ultrasound literature has shown that the ideal injectable bubble should be encapsulated and approximately the size of a blood cell (≈8 μm) to allow safe passage through the pulmonary circulation (21). Clearly, future work should involve forming this type of bubble while maintaining adequate polarization. These smaller, encapsulated bubbles would obviate the risk of embolism, which we have not addressed in this work. The low solubility of helium could raise concerns about the eventual fate of helium-filled microbubbles within the body. However, air-filled microbubbles have been safely injected in patients throughout the years (24). Nitrogen, the major component of air, is also relatively insoluble, being only 1.4 times more soluble than helium (in water at 37°C) (25). Therefore, helium should not pose much more risk than air when suspended in microbubbles. The protocols described here used proportionally larger injection volumes than would be practical for clinical use. However, increasing the bubble concentration within the fluid and achieving higher ^{3}He polarization [five-fold improvement currently possible (9)], would allow substantially less fluid to be injected. Thus, high-resolution angiographic images containing no background signal may be acquired in a biologically safe manner.

Another possible application for laser-polarized ^{3}He microbubbles is the quantitative assessment of myocardial perfusion. This has been investigated with imaging modalities such as ultrasound, nuclear medicine, and MRI (26–28). Considering cardiovascular disease is the most common cause of death in most Western countries, these studies are extremely important. Since ^{3}He is depolarized by the imaging process, multiple or longer injections can be performed without generating signal from "second pass" material. This recirculation problem can complicate or lengthen current procedures (27, 28). The extremely high signal of laser-polarized ^{3}He bubbles, along with the absence of second pass signal and lack of radiation exposure, should allow combined anatomical and functional perfusion studies that could find application in clinical diagnosis. Our preliminary results certainly encourage the development of microbubbles for delivering ^{3}He to target areas for MRI.

We thank Dr. David Needham, Dr. Chuan-Yuan Li, Dr. James MacFall, and Mr. Michael Carey (all at Duke University, Durham, NC) and Dr. Bastiaan Driehuys and Dr. Paul Bogorad (both at Magnetic Imaging Technologies, Durham, NC) for helpful discussions and technical assistance and Ms. Elaine Fitzsimons for editorial assistance. This work was supported by grants from the National Institutes of Health/National Center for Research Resources (P41 RR 05959) and the National Science Foundation (CDR-8622201). H.E.M. acknowledges a research fellowship from the Deutsche Forschungsgemeinschaft (Mo 588/3-1) and M.S.C. acknowledges a graduate fellowship from the Whitaker Foundation.

1. Happer, W., Miron, E., Schaefer, S., Schreiber, D., Wijngaarden, W. & Zeng, X. (1984) *Phys. Rev. A At. Mol. Opt. Phys.* **29,** 3092–3110.
2. Chupp, T., Wagshul, M., Coulter, K., McDonald, A. & Happer, W. (1987) *Phys. Rev. C Nucl. Phys.* **36,** 2244–2251.
3. Middleton, H., Black, R., Saam, B., Cates, G., Cofer, G., Guenther, B., Happer, W., Hedlund, L., Johnson, G., Juvan, K. & Swartz, J. (1995) *Magn. Reson. Med.* **33,** 271–275.
4. Albert, M. S., Cates, G. D., Driehuys, B., Happer, W., Saam, B., Springer, C. S., Jr., & Wishnia, A. (1994) *Nature (London)* **370,** 199–201.
5. Black, R. D., Middleton, H., Cates, G. D., Cofer, G. P., Driehuys, B., Happer, W., Hedlund, L. W., Johnson, G. A., Shattuck, M. D. & Swartz, J. (1996) *Radiology* **199,** 867–870.
6. Wagshul, M., Button, T. M., Li, H. F., Liang, Z., Springer, C. S., Zhong, K. & Wisnia, A. (1996) *Magn. Reson. Med.* **36,** 183–191.
7. Sakai, K., Bilek, A. M., Oteiza, E., Walsworth, R. L., Balamore, D., Jolesz, F. A. & Albert, M. S. (1996) *J. Magn. Reson.* **111,** 300–304.
8. MacFall, J. R., Charles, H. C., Black, R. D., Middleton, H., Swartz, J., Saam, B., Driehuys, B., Erickson, C., Happer, W., Cates, G., Johnson, G. A. & Ravin, C. E. (1996) *Radiology* **200,** 553–558.
9. Bachert, P., Schad, L. R., Bock, M., Knoop, M. V., Ebert, M., Grossman, T., Heil, W., Hofmann, D., Surkau, R. & Otten, E. W. (1996) *Magn. Reson. Med.* **36,** 192–196.
10. Kauczor, H.-U., Hofmann, D., Kreitner, K.-F., Nilgens, H., Surkau, R., Heil, W., Potthast, A., Knopp, M. V., Otten, E. W. & Thelen, M. (1996) *Radiology* **201,** 564–568.
11. Mugler, J. P., III, Driehuys, B., Brookeman, J. R., Cates, G. D., Berr, S. S., Bryant, R. G., Daniel, T. M., de Lange, E. E., Downs, J. H., III, Erickson, C. J., Happer, W., Hinton, D. P., Kassel, N. F., Maier, T., Phillips, C. D., Saam, B. T., Sauer, K. L. & Wagshul, M. E. (1997) *Magn. Reson. Med.* **37,** 809–815.
12. Bifone, A., Song, Y.-Q., Seydoux, R., Goodson, B. M., Pietrass, T., Budinger, T. F., Navon, G. & Pines, A. (1996) *Proc. Natl. Acad. Sci. USA* **93,** 12932–12936.
13. Goodson, B. M., Song, Y.-Q., Taylor, R. E., Schepkin, V. D., Brennan, K. M., Chingas, G. C., Budinger, T. F., Navon, G. & Pines, A. (1997) *Proc. Natl. Acad. Sci. USA* **94,** 14725–14729.
14. Swanson, S. D., Rosen, M. S., Agranoff, B. W., Coulter, K. P., Welsh, R. C. & Chupp, T. E. (1997) *Magn. Reson. Med.* **38,** 695–698.
15. Weathersby, P. K. & Homer, L. D. (1980) *Undersea Biomed. Res.* **7,** 277–296.
16. Saam, B., Happer, W. & Middleton, H. (1995) *Phys. Rev. A At. Mol. Opt. Phys.* **52,** 862–865.
17. Tei, C., Sakamaki, T., Shah, P. M., Meerbaum, S., Shimoura, K., Kondo, S. & Corday, E. (1983) *Circulation* **67,** 585–593.
18. Bivin, W. S., Crawford, M. P. & Brewer, N. R. (1979–80) in *The Laboratory Rat*, eds. Baker, H. J., Lindsey, J. R. & Weisbroth, S. H. (Academic, New York), Vol. 1.
19. Glover, G. H. & Pelc, N. J. (1988) *Magn. Reson. Annu.* 299–333.
20. Dumoulin, C. L., Cline, H. E., Souza, S. P., Wagle, W. A. & Walker, M. F. (1989) *Magn. Reson. Med.* **11,** 35–46.
21. Feinstein, S. B., Shah, P. M., Bing, R. J., Meerbaum, S., Corday, E., Chang, B. L., Santillan, G. & Fujibayashi, Y. (1984) *J. Am. Coll. Cardiol.* **4,** 595–600.
22. Johnson, G. A., Chen, X. J., Cates, G., Cofer, G. P., Driehuys, B., Hedlund, L. W., Happer, W., Saam, B., Shattuck, M. D. & Swartz, J. (1997) *Magn. Res. Med.* **38,** 66–71.
23. Chen, X. J., Chawla, M. S., Hedlund, L. W., Möller, H. E., MacFall, J. R. & Johnson, G. A. (1998) *Magn. Reson. Med.* **39,** 79–84.
24. Christiansen, C., Kryvi, H., Sontum, P. C. & Skotland, T. (1994) *Biotechnol. Appl. Biochem.* **19,** 307–320.
25. Verstappen, F. T., Bernards, J. A. & Kreuzer, F. (1977) *Pflügers Arch.* **368,** 89–96.
26. Winkelmann, J. W., Kenner, M. D., Dave, R., Chandwaney, R. H. & Feinstein, S. B. (1994) *Ultrasound Med. Biol.* **20,** 507–515.
27. Sodee, D. B., Port, S. C., O'Donnell, J. K., Khaw, B. A., Narula, J., Yasuda, T. & Strauss, H. W. (1995) in *Principles and Practice of Nuclear Medicine*, eds. Early, P. J. & Sodee, D. B. (Mosby, St. Louis), pp. 370–442.
28. Wilke, N., Jerosch-Herold, M., Stillman, A. E., Kroll, K., Tsekos, N., Merkle, H., Parrish, T., Hu, X., Wang, Y., Bassingthwaighte, J., *et al.* (1994) *Magn. Reson. Q.* **10,** 249–286.